Electrochemistry Communications 166 (2024) 107792

Contents lists available at ScienceDirect

Electrochemistry Communications

journal homepage: www.elsevier.com/locate/elecom

Systematic study of the N concentration effects on metal-free ORR electrocatalysts derived from corncob: Less is more

J.C. Martínez-Loyola [a], M.A. Carrasco-Cordero [b], I.L. Alonso-Lemus [c], F.J. Rodríguez-Varela [d,e], P. Bartolo-Pérez [f], B. Escobar-Morales [g], Y.I. Vega-Cantú [a,h], F.J. Rodríguez-Macías [a,h,*]

[a] Tecnologico de Monterrey, Escuela de Ingeniería y Ciencias, Ave. Eugenio Garza Sada 2501 Sur, Col: Tecnológico, Monterrey, NL, Mexico 64700
[b] Escuela Superior Politécnica de Litoral, Km 30.5 Vía Perimetral 090902, Gye, Ecuador
[c] CONAHCyT, Sustentabilidad de los Recursos Naturales y Energía, Cinvestav Unidad Saltillo, Ramos Arizpe, Coah. 25900, Mexico
[d] Sustentabilidad de los Recursos Naturales y Energía, Cinvestav Unidad Saltillo, Parque Industrial Ramos Arizpe, Ramos Arizpe, Coah. 25900, Mexico
[e] Nanociencias y Nanotecnología, Cinvestav Unidad Saltillo, Mexico
[f] Cinvestav Unidad Mérida, A.P. 73 Cordemex, Mérida, Yucatán, Mexico
[g] CONAHCYT, Centro de Investigación Científica de Yucatán, Carretera Sierra Papacal-Chuburná Puerto, Km 5 97302, Mérida, Yucatán, Mexico
[h] Pós-Graduação em Ciência de Materiais, Universidade Federal de Pernambuco, Av. Prof. Moraes Rego 1235, Cidade Universitária, Recife 50.670-901, PE, Brazil

ARTICLE INFO

Keywords:
Corncob biomass waste
Metal-free porous carbons
Urea doping
Oxygen reduction reaction

ABSTRACT

We report nitrogen-doped biomass-derived porous carbon materials with great performance for the Oxygen Reduction Reaction (ORR) in alkaline media. The level of nitrogen doping in a simple pyrolysis of corncob (CC) was varied systematically, a 1:1 CC:urea ratio (CC_{1U}) gave the best performance in terms of onset potential (E_{onset} = 0.97 V vs. RHE), maximum current density (j_{max} = -3.22 mA cm^{-2}), hydroperoxide ion yield (%HO_2^- = 1.18 % at 0.5 V), and electron transfer number (n = 3.86 at 0.5 V). Unexpectedly, for higher CC:urea ratios the doping decreases, instead of plateauing, with lower concentration of C-N sites and more sp^2 sites as determined by XPS, as well as lower specific surface area (SSA), while increasing both porosity and carbon (0 0 2) interplanar distance ($d_{(002)}$). These materials should be durable and robust, since their performance actually improved after accelerated degradation tests. This study proves that renewable "waste" can be upconverted into metal-free electrocatalysts for electrochemical energy conversion technologies and emphasizes the need for studying and controlling doping levels to enhance performance.

1. Introduction

Anion Exchange Membrane Fuel Cells (AEMFCs) have several economic, environmental, and engineering advantages compared to energy systems functioning with fossil fuels, and even with respect to the more common Proton Exchange Membrane Fuel Cells (PEMFCs) counterpart. For example, the operating atmosphere is less corrosive, cheap metal-free electrocatalysts can be used as cathodes, and the kinetics of the ORR has been reported to be faster in alkaline media compared to acid conditions [1]. However, the ORR is about three orders of magnitude kinetically slower than the hydrogen oxidation reaction (HOR) at the anode of AEMFCs, limiting their overall performance [2]. Therefore, it is fundamental to develop highly active electrocatalysts for the ORR [3]. It is well known that the ORR can proceed by a one-step mechanism, i.e. that following a $4e^-$ transfer pathway (1) [4,5], or by an indirect mechanism, involving a $2e^-$ pathway (2). The former is preferable since it avoids the generation of the undesired HO_2^- reaction intermediate (3) [6–9].

$$O_2 + 2H_2O + 4e^- \rightarrow 4OH^- \quad (1)$$

$$O_2 + H_2O + 2e^- \rightarrow OH^- + HO_2^- \quad (2)$$

$$HO_2^- + H_2O + 2e^- \rightarrow 3OH^- \quad (3)$$

Since they are relatively inexpensive, heteroatom-doped carbon materials are among the most promising alternative electrocatalysts for the ORR, with the potential to replace noble-metal based electrocatalysts [1,10]. In this regard, porous carbons (PCs) have attracted tremendous attention because their physicochemical and textural properties facilitate the adsorption and diffusion of species, also

* Corresponding author.
E-mail address: fernando.jrm@tec.mx (F.J. Rodríguez-Macías).

https://doi.org/10.1016/j.elecom.2024.107792
Received 24 June 2024; Received in revised form 22 July 2024; Accepted 28 July 2024
Available online 29 July 2024

showing good chemical stability, and excellent electrical–mechanical properties [11–13]. Substitutional heteroatom doping of PCs (e.g., with S, P, B, N) enhances their electrical conductivity and modifies their surface chemical properties [14]. Some heteroatoms-doped PCs even show higher catalytic activity for the ORR than conventional Pt/C electrocatalysts [15–17]. Thus far, nitrogen is the most widely studied doping heteroatom; however, the specific contribution of each active N-species (e.g.; N-graphitic, N-pyridinic, N-pyrrolic, oxidized) on the catalytic activity of PCs for the ORR is still under discussion [18,19].

As a low-cost alternative to conventional nanostructured carbons, many sources of biomass have been processed into PCs, including wheat [20], orange peel [21], soybean [22], banana peel [23], onion peel [24], and rice [25]; more examples can be found elsewhere [26]. This approach offers several environmental advantages, since biomass is abundant, inexpensive, easily accessible, and its exploitation can promote the use of renewable sources [27,28]. Over the past decade, newly designed metal-free and low-cost green electrocatalysts have been processed from biomass, becoming fundamental to advance in the large-scale commercialization of high performance, non-polluting electrochemical devices, such as AEMFCs.

On this matter, corn is an abundant source of biomass. Approximately 1,224.8 million metric tons of corn will be produced in 2024 according to the U.S. Department of Agriculture [29]. The eight major producers and exporters of corn are the United States, China, Brazil, the European Union, Argentina, India, Ukraine and México [30]. México alone produced 27 million tons of corn in 2021 [31] and 25.5 million metric tons in the 2023/24 market year [30], which is supplemented by imports to provide for an annual consumption of ca. 335.2 kg per capita in 2023 [32]. After the extraction of corn kernels, CC is the waste remaining [33], representing about 20 % of the total grain biomass [34]. CC has been widely used for heating, as desiccant and adsorbent, and as additive, among other applications [35]. However, the sustainable management of this agricultural waste, and its conversion into value added products, still present opportunities for the scientific community.

CC has been used as precursor to mesoporous carbons, with good performance for the ORR after addition of metals. Sahu et al. showed that N and F doping of carbon from CC promotes the ORR by modifying their structural and textural properties and developing active sites [36]. Moreover, adding metals such as Fe and Co enhances catalytic activity. For example, Jiang et al. encapsulated Fe_2O_3 nanocrystals within CC-derived carbon nanofibers [37], showing 91 % current density retention after 10,000 s. The catalytic activity for the ORR has been attributed to the well dispersed Fe compounds over the N-doped carbon matrix. Chen et al., incorporated Co, P, N, and O into the framework of a CC-derived carbon [38]. The authors report high catalytic activity for the ORR, due to heteroatom doping, high specific surface area, and the development of Co_2O_3/$Co_2N_{0.67}$ sites. Table 1 summarizes other examples, showing that preparing ORR active carbon from biomass is a popular approach, but metal-free electrocatalysts have received less attention and CC has not been studied for this.

Eliminating the need for metals, by taking advantage of catalytic sites introduced by doping of carbon could be advantageous, making biomass derived electrocatalysts less expensive and easier to produce than their metal-enhanced counterparts. The effect of doping with heteroatoms, such as N, in ORR performance is well-known [46], but, research on how the concentration of the heteroatom influences ORR performance and other physicochemical parameters of PCs is scarce and has not yet been reported for carbon catalysts from CC or other biomass precursors.

In this context, we present a novel and systematic study of the effects of varying N concentration in CC-based electrocatalysts. We report a process to dope PCs derived from CC with N-species and evaluate their performance for the ORR as function of dopant. To the best of our knowledge, this is the first-time that N-doped PCs electrocatalysts have been produced from CC, showing good performance while remaining metal-free. Several CC:urea (as source of the N-species) mass ratios are evaluated. The catalytic activity for the ORR of the resulting CC-based electrocatalysts is characterized before and after an Accelerated Degradation Test (ADT). This work provides alternatives to modifying the carbon matrix with metals or different heteroatoms to activate ORR. Additionally, it provides a broader perspective of the advantages of designing PCs from abundant biomass and using them as electrocatalysts in electrochemical energy conversion devices. We aim to demonstrate that agro-industrial waste can be transformed into active ORR electrocatalysts at low cost, using easily accessible reagents, and simple methodologies.

Table 1
Recent examples of PCs from biomass and their use as ORR electrocatalysts.

Precursor	Heteroatom	Metals/ agents used	Approach	ORR performance	Ref.
Pea pods	–	ZnX_2 (X=F, Br, I, Cl).	Study the use of different zinc halides.	$E_{onset} = 0.97$ $n = 3.99$	[39]
Rice husk	N	Fe, Si	Study effects of NaOH amount, temperature, and time.	$E_{onset} = 0.96$ $n = 3.66$	[40]
Rattan tea	N, P	Fe, Ni	Effect of Fe:Ni ratios (Ni fixed).	E_{onset}= (NR) $n = 3.95$	[41]
Chitosan	N, P	Co	Study the effects of phytic acid and acetic acid.	(NR)	[42]
PAN	N	–	Study the effects of ultrasonic treatment time.	(NR)	[43]
Corn stalk	N	Fe	Study the effects of corn stalk binder wt % and Fe.	$E_{onset} = 1.01$ n= (NR)	[44]
Eucalyptus pulp	N	Fe	Study the effects of carbonization temperature.	$E_{onset} = 0.90$ n= (NR)	[45]
Corncob	N	–	Study the effects of different N amounts.	$E_{onset} = 0.97$ $n = 3.97$	This work

E_{onset}: onset potential; n = electron transfer number; (NR)*: not reported.*

2. Experimental

2.1. Materials

All reagents were used as received without additional purification: KOH (90 %), 2-propanol (<99.5 %), and Nafion® 117 solution (5 wt%) were purchased from Sigma Aldrich. Urea (99 %) was acquired from J.T. Baker. Ultra-high purity (UHP, 99.999 %) N_2 and O_2 were supplied by Infra. *Celaya* corn was collected from a local market in Monterrey, México.

2.2. Synthesis of PCs

CC samples were cut in cubes of approximately 1 cm^3, washed thoroughly with distilled water, and sun-dried for 72 h, followed by heat treatment in air atmosphere at 180 °C for 2 h to facilitate manual grinding. The CC powders were sieved and precarbonized in a tubular furnace at 400 °C for 2 h with a heating rate of 5 °C min^{-1} and a N_2 flow rate of 40 mL min^{-1}.

Afterwards, mixtures of CC and KOH as activating agent in a 1:3 wt ratio, and urea as source of nitrogen, were prepared. CC:urea wt. ratios

of 1:1, 1:2, 1:3, and 1:4 were adjusted. The mixtures were separately added to 50 mL of distilled water, vigorously stirred for 24 h at 50 °C, and dried at 100 °C until solvent evaporation. The dried mixtures were pyrolyzed in a tubular furnace at 800 °C for 1 h with a N_2 flow rate of 40 mL min^{-1} and a heating rate of 5 °C min^{-1}. The carbon materials were washed with distilled water until a neutral pH was achieved, vacuum filtered (2 μm pore diameter Whatman filters), and dried overnight at 80 °C. The resulting electrocatalysts were labeled as CC_{XU} where XU represents the urea ratio (e.g., CC_{1U} indicates synthesis using the CC: urea wt. ratio of 1:1). The non-doped CC_0 electrocatalysts was synthesized following the same procedure, avoiding the addition of urea. The synthesis conditions were chosen considering several studies summarized by Sumangala et al [47].

2.3. Physicochemical characterization

X-ray diffraction (XRD) patterns were obtained in a Bruker D2Phaser diffractometer (Cu-Kα radiation source, λ = 1.518 Å) using a 10-99° 2θ scale range and a step size of 0.01°. ATR-FTIR spectra were acquired using a PerkinElmer Spectrum 400 equipment in the 500–4000 cm^{-1} wavelength range, with a resolution of 4 cm^{-1}. Raman spectra were collected in a Thermo-Scientific DXR spectrometer with a 633 nm laser and in the 3500–200 cm^{-1} Raman shift range and 100 scans. N_2 adsorption and desorption analysis was done using a Quantachrome Nova 2200 equipment. The morphology, elemental chemical composition and mapping were performed using a JEOL JSM 7800f Prime FESEM apparatus, operating with 5 kV accelerating voltage. The HRTEM images were acquired with a FEI Talos F200 microscope. Elemental mapping by Energy Dispersive X-ray spectroscopy (EDS) was performed in HAADF-STEM mode, at 30 kV. Distances in the electron micrographs were measured with the ImageJ software. Surface chemical surface composition was studied by X-ray photoelectron spectroscopy (XPS) with a Thermo Scientific K-Alpha spectrometer, using an X-Ray source of Al K_α (1486.6 eV) on a 400 μm wide oval spot, after sputter cleaning by Ar^+ beam (3 kV, 15 s). High-resolution regions were acquired with 50 eV of pass energy and 50 ms of dwell time. Deconvolutions were realized using the Shirley-Sherwood method and binding energies were calibrated to 284.8 eV (C 1 s peak).

2.4. Electrochemical characterization

Best practices for ORR performance determination were considered in the electrochemical characterization of this work [48]. All the electrochemical characterization was evaluated in a three-electrode cell configuration using a Bio-Logic VSP-300 bipotentiostat coupled to a Rotating Ring Disk Electrode (RRDE) set-up (Pine Research Instrumentation). An Ag/AgCl reference electrode (RE) in saturated KCl solution was placed into a Luggin capillary and used during the tests. The counter electrode was a graphite bar also introduced into a Luggin capillary. The electrolyte used for all measurements was 0.1 mol/L KOH and all the potentials have been referred to the Reversible Hydrogen Electrode (RHE). The work electrode (WE) was a glassy carbon (diameter = 5.61 mm), with a gold ring (Pine Res. Inst.). The catalyst inks were prepared by mixing 10 mg of the electrocatalyst, 1 mL of 2-propanol, and 30 μL of Nafion®. The mixture was dispersed by ultrasound for 30 min. Then, 4 aliquots of 3 μL were deposited on the glassy carbon to produce the WE.

The ORR activity was determined following the next protocol: i) Activation (40 cycles, 50 mV s^{-1} in N_2-saturated electrolyte), ii) cyclic voltammograms (CVs) at scan rate of 20 mV s^{-1} in N_2-saturated electrolyte, iii) background current determination (scan rate of 5 mV s^{-1} at 1600 rpm in N_2-saturated electrolyte); iv) Linear sweep voltammograms (LSVs) at several rotation rates (ω = 200, 400, 800, 1200, and 1600 rpm) and 5 mV s^{-1} in O_2 saturated electrolyte; and v) ADT carried out following the recommendations of the US Department of Energy (DOE) [49], i.e., 3000 cycles at 50 mV s^{-1} in N_2 atmosphere. Activation, CVs, background current, and LSVs were performed in a window potential between of 0.05 and 1.2 V vs. RHE, while ADT in the 0.6 to 1 V vs. RHE range. The current density (*j*) was obtained considering the geometric area of the WE.

During the ORR measurements, the Au ring was polarized at 1.2 V vs. RHE to sense the ring current (I_R). The HO_2^- intermediate yield (%HO_2^-) and the electron transfer number (n) were determined before and after ADT with Equations (4) and (5) respectively [50]:

$$\%HO_2^- = \frac{\frac{200*I_R}{N}}{I_D + (\frac{I_R}{N})} \quad (4)$$

$$n = \frac{4*I_D}{I_D + (\frac{I_R}{N})} \quad (5)$$

where I_D is the disk current, and N is the collection efficiency provided by the manufacturer (0.37).

3. Results and discussion

3.1. Physicochemical characterization

The broad and low intensity peaks of the XRD patterns of the electrocatalysts, in Fig. 1 a), indicate a high content of disordered structures, however, two maxima can be identified at ~23° and ~44° (2θ), corresponding to the (002) and (100) carbon reflections (JCPDS no. 41–1487) [51]. It should be noted that the (002) peak slightly shifts towards smaller angles as the urea concentration increases (Fig. 1 b) compared to non-doped CC_0, due to structural modifications of the carbon. This would correspond to an increased interplanar spacing, $d_{(002)}$, with higher CC:urea ratio [52]. The calculated values of $d_{(002)}$ are shown in table S1.

Since the (002) peak is related to the orientation of carbon layers in a

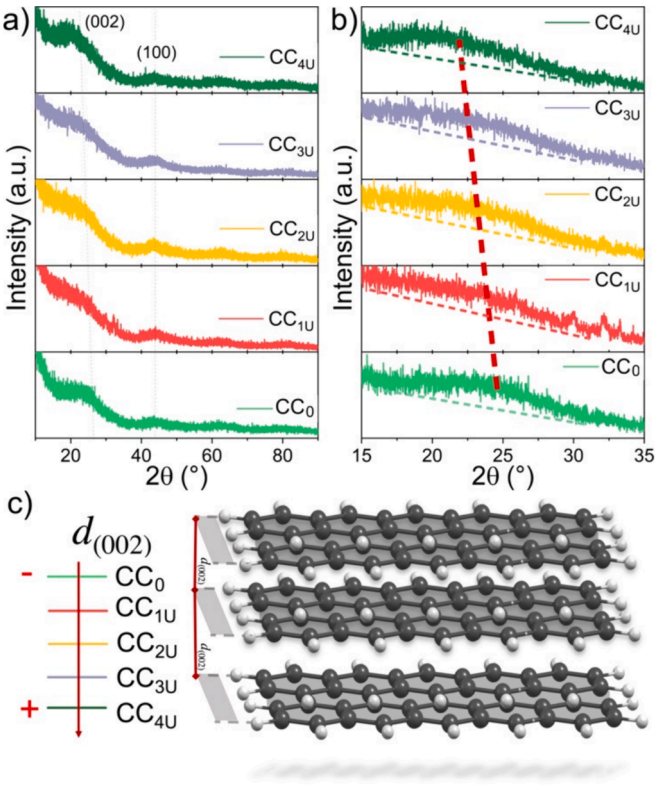

Fig. 1. a-b) XRD patterns and zoom of the 15-35° 2θ interval of the electrocatalysts, respectively; and c) scheme of the $d_{(002)}$ expansion as a function of the urea content, where the black and white spheres represents carbon and hydrogen atoms, respectively.

3D matrix [53], these results indicate that the urea concentration also has an important effect on the average distance between graphite layers (schematized in Fig. 1 c), with the planes becoming further separated as more urea is added, indicating a less graphitized and more amorphous structure.

The FTIR spectra of the electrocatalyst (Figure S1) shows several bands between 2500 and 750 cm^{-1}: CC_0 has signals in 2153 cm^{-1}, 1956 cm^{-1}, 1733 cm^{-1}, and 969 cm^{-1} which correspond to C=C=O and C=O stretching, and C=C bending [54]. The C=C band remain in the doped samples, CC_{1U} and CC_{2U} together with new bands at 1841 cm^{-1}, 2116 cm^{-1} and 2333 cm^{-1} corresponding to N=C=N bending and C=O stretching, respectively [55]. This indicates formation of graphitic C=N surface bonds [56]. These doped CC also show C–H signals around 1500 cm^{-1} and another C=N band at 1000 cm^{-1}.

With a higher dopant level, in samples CC_{3U} and CC_{4U}, peaks related to the C–H bond appear between 1405–1572 cm^{-1} [57]. Additionally, the signal at 969 cm^{-1} widens to 1121 cm^{-1} suggesting the presence of O=C-N stretching species instead of C=N bonds as in CC_{2U}; these signals have been related to pyridinic-N bond in PC electrocatalysts [58]. However, around 1750 cm^{-1} CC_{3U} show C=O signals while CC_{4U} has N=C=N bonds. These results suggest that an increase in the CC:urea (2 and 3 ratios) may hinder the formation of active C-N species over the electrocatalysts surface [59].

Fig. 2 a) shows the Raman spectra of the electrocatalysts, with the well-known D (~1335 cm^{-1}, sp^3 carbon hybridization, or "defects") and G (~1565 cm^{-1}, sp^2 carbon, or "graphitic") [60]. Both bands are broad and overlap, indicating a high amount of amorphous carbon structures. The graphitization degree of carbon materials can be estimated by the I_D/I_G intensity ratio, a decrease in this ratio has also been related to a rearrangement of edge-bonded graphitic sites [61].

The broad bands include contributions from D*, D', and D" inter-bands, related to carbon–oxygen interactions from the carbon matrix [62]. Deconvolution shows the relative contributions of the five bands, in Fig. 2 b and c) for CC_0 and CC_{1U}. The other doped CC_{2U}, CC_{3U}, and CC_{4U} are substantially similar to CC_{1U} and are depicted in Supplementary Figures S2 a-c). Deconvolution allows to find more accurate values for the D and G bands, to calculate I_D/I_G (shown in table S1). The I_D/I_G value of CC_0 is 1.86, for the lowest doping it is 1.73, and it decreases further as the CC:urea ratio increases, with a minimum of 1.30 for CC_{3U}, followed by a slight increase to 1.42 for CC_{4U}. This trend suggests that the N-doping promotes the graphitization of the electrocatalysts, which increases with higher urea content. Raman spectra also show 2D and D+G bands, related to carbon lattice defects promoted by O and N atoms [63] for CC_{1U} and CC_{2U}. These bands do not appear for CC_{3U}, and CC_4, which might be due to the decrease of C=O interaction. From the spectroscopy analysis we propose there is a structural differences between CC_0 and CC_{1U}, with the CC:urea 1:1 ratio promoting C-N and C=C bonds a less C=O bonding, this is schematized in Fig. 2 d).

The doping level also affected porosity. The specific surface area (also shown in Table S1), measured by N_2 adsorption and desorption analysis, shows a value of 4.4 m^2/g for the undoped material (CC_0) this increases almost 400 times with doping to a value of 1682.34 m^2/g for CC_{1U}. With higher amounts of urea, SSA decreases to 449.53, 259.37, and 220.75 m^2/g for CC_{2U}, CC_{3U}, and CC_{4U}, respectively. These results are consistent with our interpretation that adding more urea promotes graphitization. The high SSA of CC_{1U} is related to a large number of pores and channels for ion diffusion which should increase electrochemical performance [64], and hint that this material should show the best performance.

Fig. 3 shows FESEM micrographs of the electrocatalysts. CC_0 shows large, smooth particles of irregular shape (Fig. 3 a). Fig. 3 b) shows the morphology of CC_{1U} with large pores, up to 1.4–1.5 μm, as an effect of the urea doping. The observed pore size decreases in CC_{2U} and CC_{3U} (Fig. 3 c and d). The showed cavities might be due to impregnation of urea into the carbon matrix, since urea has been reported to act as a shape directing agent by producing gases (NH_3) promoting the

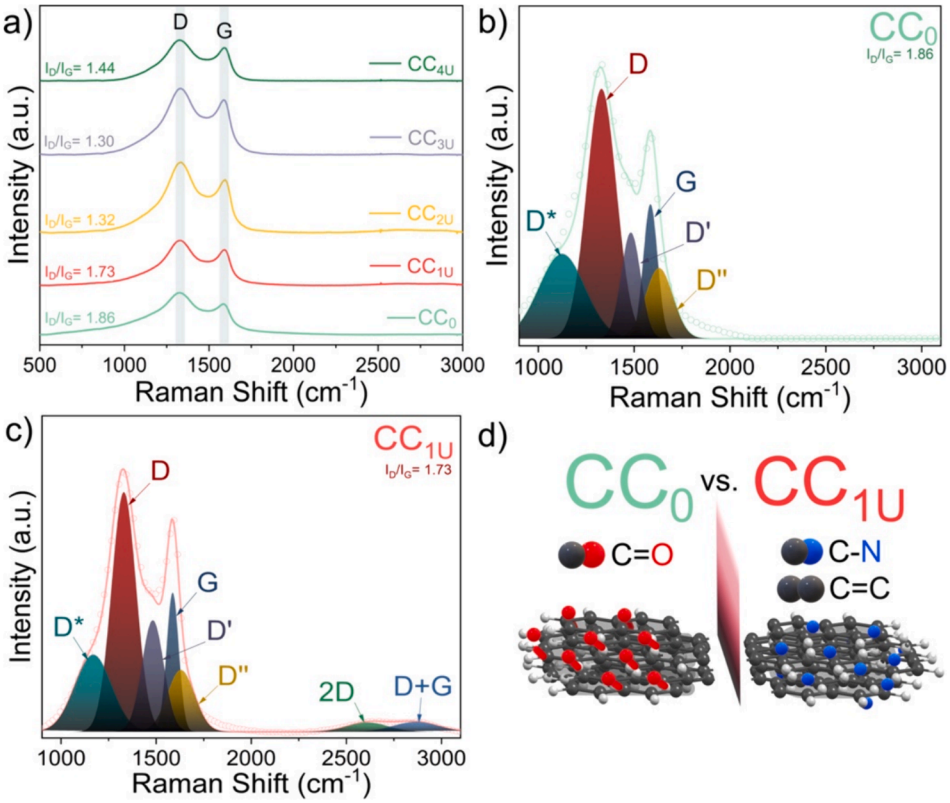

Fig. 2. a) Raman spectra of the electrocatalysts; b-c) deconvoluted Raman spectra of CC_0 and CC_{1U} respectively; and d) illustration of the main structural differences between CC_0 and CC_{1U}.

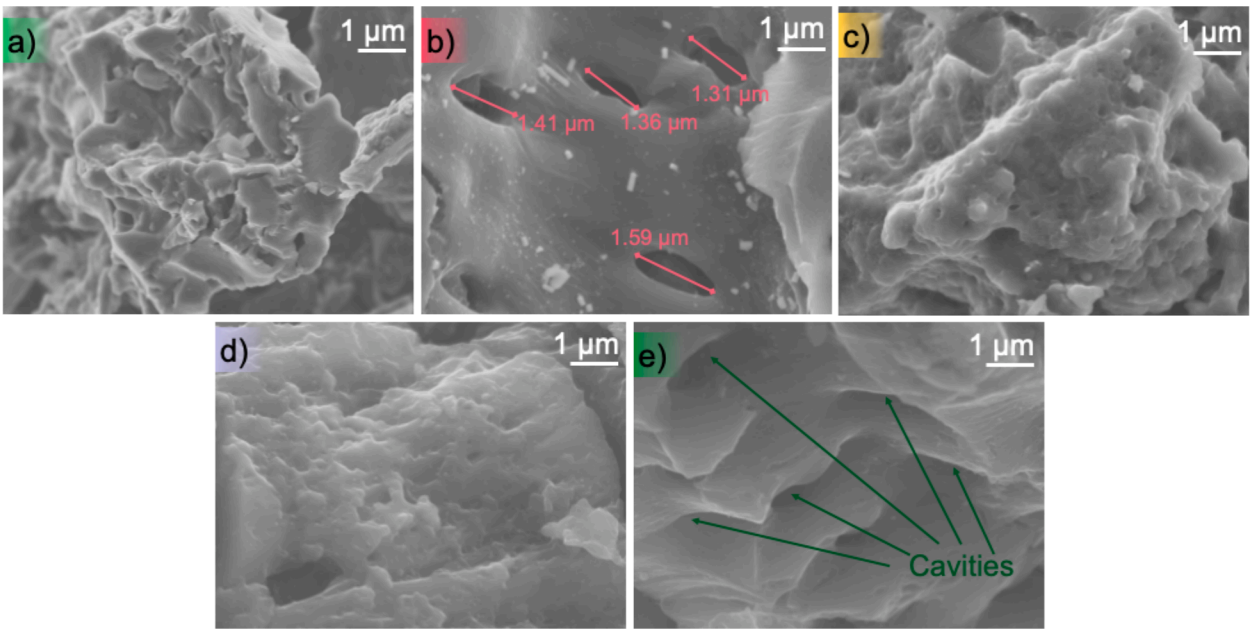

Fig. 3. FESEM images of a) CC_0, b) CC_{1U}, c) CC_{2U}, d) CC_{3U}, and e) CC_{4U}.

formation of micro/mesopores [65], the presence of which promotes the highest specific surface area and storage/transport of ions [66,67]. While relatively large cavities are observed in CC_{4U} (Fig. 3 e), the number of mesopores would still decrease according to SSA measurements, suggesting that the reduction in porosity due to graphitization has a larger effect than the observed microscale roughness.

Elemental mapping by EDS and more FESEM micrographs are shown in Figure S3, in addition to C, elemental analysis showed O, Ca, and P in all samples, the amounts are shown in in Table S2. Nitrogen was not detected in the undoped sample, but it does show clearly in the doped samples, and mapping reveals that it is very well distributed. The amounts of nitrogen decrease as more urea was used in the porous CC materials synthesis, suggesting that excess urea inhibits the formation of C-N bonds. This may be attributed to remotion of unreacted nitrogen due to the low diffusion of N atoms into the carbon structure [68]. This decrease in nitrogen concentration is again consistent with the Raman results above, the presence of nitrogen increases the intensity of the D peak, but both I_D/I_G and at% of nitrogen go down when more urea is used. Ca and P are also detected, which is to be expected since these are common elements in biomass, including CC [69]. Higher concentrations of Ca and P in some spots in the map suggest that some calcium phosphate forms after calcination, which makes us hypothesize that P doping is not significant, but they also appear independent of each other in the map, and their total concentration is not fully correlated.

Fig. 4 a) shows a bright field HRTEM micrograph of CC_{1U}. Fig. 4 b) is a zoom of the area highlighted by the yellow square in Fig. 4 a). Some curved and non-aligned carbon domains are observed, which are characteristic of a disordered hard carbon material [70], which has been reported before for other biomass-derived porous carbons [71]. The interlayer spacing of CC_{1U} is around 0.36–0.4 nm, ascribed to the (0 0 2) carbon plane [72]. The porous network of CC_{1U} is confirmed in Fig. 4 c), where pores are distributed in the carbon matrix [73]. The HAADF-STEM micrograph and chemical mapping of CC_{1U} in Fig. 4 d) shows C, O, and N homogeneously dispersed over the carbon surface, suggesting its successful doping.

Additional HRTEM images are shown in the supporting information for CC_0 (Fig. S4), CC_{2U} (Fig. S5), CC_{3U} (Fig. 6), and CC_{4U} (Fig. S7), together with dark-field images and EDS mappings. N does not show in the EDS map for CC_0 (fig. S4 c), but in all the doped materials N and O are homogenously dispersed in the carbon material. The materials with more doping do not show partially graphitized domains like the ones seen for CC_{1U}, which would mean that they are more likely to be soft carbon. It important to mention that, even though hard and soft carbon look different in HRTEM images, both may have identical XRD patterns and Raman spectra [70]. These results indicate that CC:urea 1:1 ratio promotes hard carbon alignment.

An XPS survey scan, shown in Fig. 5 a), confirms the presence of O and N species for the doped electrocatalysts. The XPS quantification is shown in Table 2. The nitrogen content of the undoped material is quite low, below what could be easily detected by EDS. Confirming what has been discussed above, N content is highest for CC_{1U}, but decreases as the CC:urea ratio increases.

High resolution XPS for the C 1 s region of CC_0 (Fig. 5 b) shows sp^2 and sp^3 bonding (284.7 and 285.3 eV binding energies respectively, [74]), as well as C-O-C (286.7 eV) and C-O (285.9 eV), bonds. The O 1 s high resolution spectrum corroborates the presence of C-O bonds (533.1 eV) and also shows a significant amount of C=O bonds (531.5 eV) [75].

For the CC_1 doped carbon, high resolution XPS (Fig. 5 c) also shows C-OH in the C 1 s peak (at 285.5 eV), and in the O 1 s peak. More significantly C=N bonds (284.1 eV, [76]), which are absent in CC_0 are prominent in the deconvolution. The C-N bonding is confirmed in the N 1 s peak, which shows N species with pyridinic, pyrrolic, and graphitic bonding at 398.1, 399.3, and 400.8 eV respectively [77].

The high-resolution XPS spectra for the N 1 s, C 1 s, and O 1 s regions of CC_{2U}, CC_{3U}, and CC_{4U} are shown in supplementary Figures S8-S10, respectively. The relative concentrations of the different types of bonds for the undoped and doped carbons are also shown in the supporting information, in Table S3. The other doped carbons also show the pyridinic, pyrrolic and graphitic C-N bonds, but the two samples treated with higher urea amounts, CC_{3U}, and CC_{4U}, also show oxidized nitrogen, the appearance of which is correlated mostly to a decrease in pyrrolic-N. Apart from this, the rest of the species at the C 1 s and O 1 s regions are the same as those identified at CC_{1U}. The relative concentration of the different bondings in Table S3 shows that the increase in CC:urea has the following effects: i) promote the formation of N-oxidized species; ii) inhibit the formation of C-OH functional groups; and iii) decrease the relative concentration of pyrrolic-N, while increasing that of pyridinic-N. However, it has a limited effect on the concentration of C-O and C=O species.

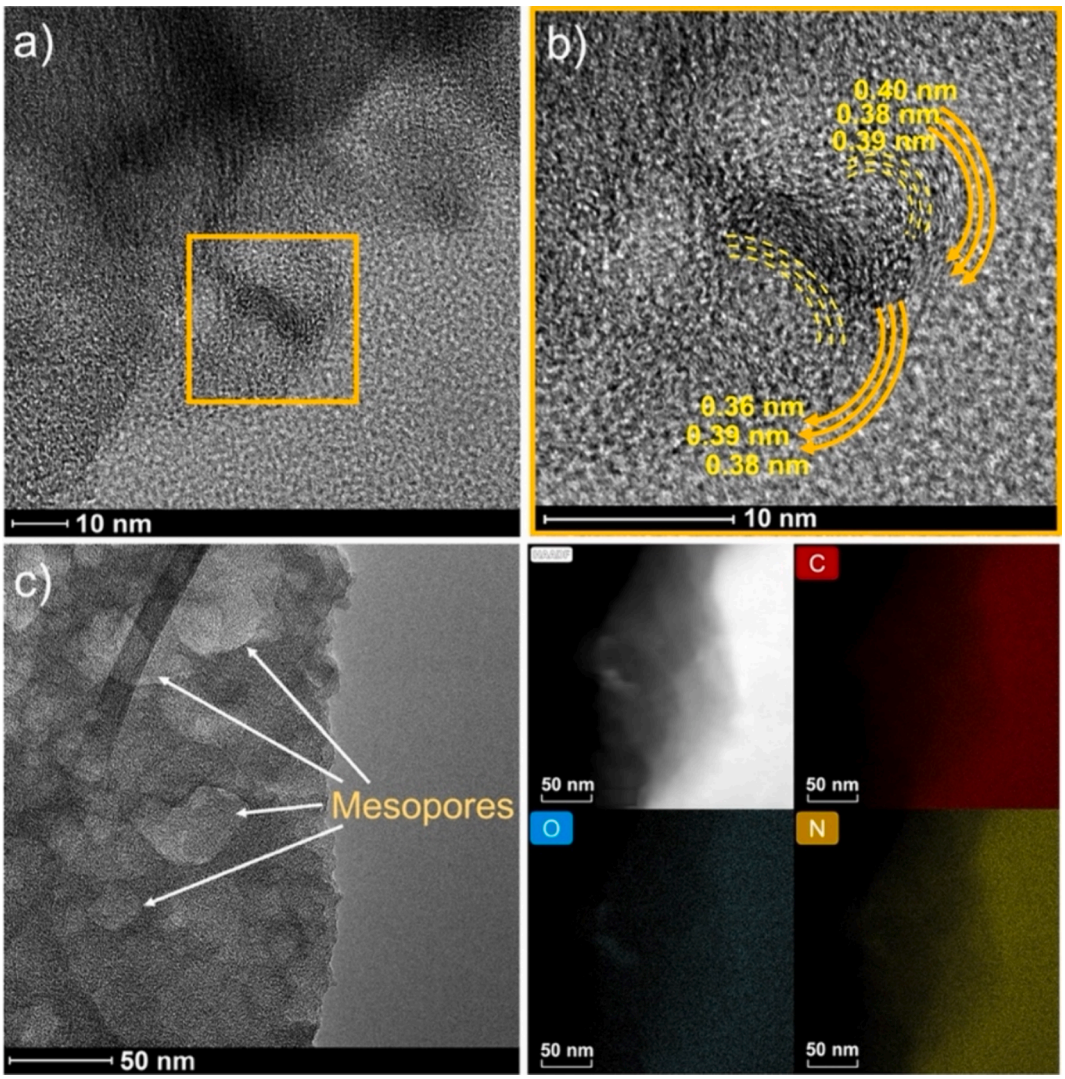

Fig. 4. a) HRTEM micrograph of cc_{1U}, the area marked by the yellow square is shown in b), where curved graphitic sheets can be identified, this electrocatalyst material has mesopores, as shown in c), EDS mapping, in HAADF-STEM mode, of the CC_{1U} material shown in d) reveals that nitrogen is very well distributed, together with oxygen. (For interpretation of the references to colour in this figure legend, the reader is referred to the web version of this article.)

3.2. Catalytic activity for the ORR

Fig. 6 a) shows the CVs of CC_0, CC_{1U}, CC_{2U}, CC_{3U}, and CC_{4U}, which have a semi-capacitive behavior, with the higher *j* values generated by the electrocatalysts doped with CC:urea ratios of 1:2, 1:3, and 1:4, ascribed to their high specific surface area that promotes electrolyte storage, ion diffusion, and fast charge transfer [78]. The shape of the CV corresponding to CC_{1U}, stands out, with a more quasi-rectangular profile, suggesting an electrochemical surface area available without Faradaic peaks [79]. Moreover, only CC_{1U} shows a well-defined cathodic peak with an onset potential at 0.88 V vs. RHE. The appearance of such peak is typically attributed to the reduction of oxygenated absorbed species (highlighted circle in Fig. 6 a) [80]. Overall, the shape of the CVs shown by the CC-based electrocatalysts (i.e., a double-layer capacitance behavior) is expected, since a capacitive behavior results from highly porous materials [81,82]. For comparison, the CV of a commercial 20 wt % Pt/C electrocatalyst is also shown in the Fig. 6 a), showing its characteristic shape in alkaline electrolyte.

The Linear Sweep Voltammograms of the electrocatalysts (at 1600 rpm, before ADT) are shown in Fig. 6 b). The N-doped electrocatalysts have a more positive E_{onset}, compared to CC_0, in the order CC_{1U}>CC_{2U}>CC_{4U}>CC_{3U} (Table 3). The E_{onset} of CC_{1U} is only 20 mV more negative than that of Pt/C (0.97 vs. 0.99 V vs. RHE). CC_{1U} also has the more positive $E_{1/2}$ among the carbon electrocatalysts: 0.70 V vs. RHE (150 mV difference from Pt/C before ADT). CC_{1U} delivers a j_{max} of -3.22 mA cm^{-2}, lower than -4.07 mA cm^{-2} of CC_{2U} before ADT (Table 3). It is important to emphasize that although the kinetic, mixed, and diffusion regions in the LSV curves of the CC-based electrocatalysts are not as well-defined as in Pt/C, the E_{onset} and $E_{1/2}$ values are improved by the doping of the carbon structure.

P-heteroatom doping of porous carbon has also been reported as a promoter of the catalytic activity for the ORR of PCs [51]. Even though P was not detected in our XPS survey scan, EDS (Figure S3) showed its presence in the CC electrocatalysts, however no significant difference in P content between CC_0 and CC_{1U} was observed (see Table S2), while the difference in N content is notorious both in EDS and XPS quantifications. Thus, the noticeable difference in ORR activity between CC_0 and CC_{1U} is attributed to N-doping, and any effect of P on the performance of the CC electrocatalysts is considered negligible.

The ADT provides relevant information of the electrochemical stability of fuel cell electrocatalysts. Often, a decrease in E_{onset}, $E_{1/2}$, and j_{max} is observed after cycling. For instance, the metal-free carbon semitubes prepared by Zhang et al. showed an 8 mV negative shift of $E_{1/2}$ after 5,000 cycles [68]. Wang et al. synthesized a metal-free N, S co-

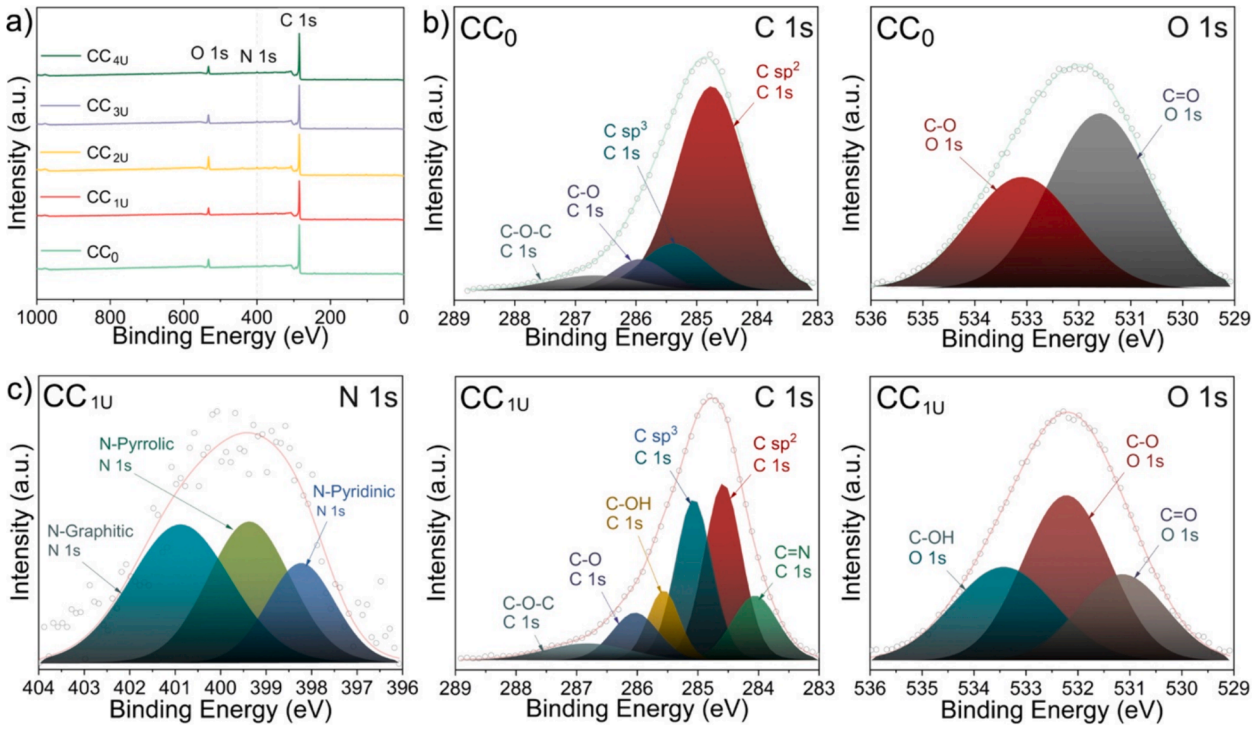

Fig. 5. a) Survey XPS scan of the electrocatalysts; b) high-resolution spectra of the C 1 s and O 1 s regions of CC_0; c) high-resolution spectra of the N 1 s, C 1 s, and O 1 s of CC_{1U}.

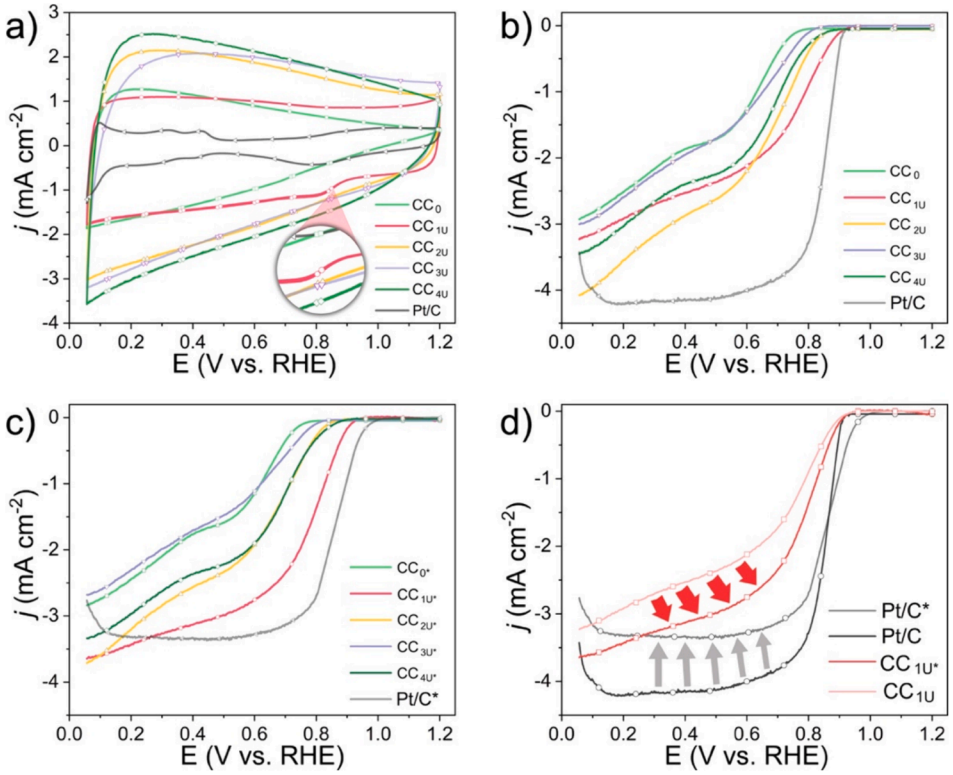

Fig. 6. a) CVs of the electrocatalysts acquired at 20 mV s^{-1} in N_2-saturated 0.1 mol/L electrolyte; b) LSVs of the ORR before ADT of the electrocatalysts at 1600 rpm, 5 mV s^{-1}, and O_2-saturation conditions; c) LSVs after ADT of the electrocatalysts, same conditions as in b); and d) comparison of catalytic activity for the ORR before and after ADT of CC_{1U} and Pt/C at 1600 rpm.

doped mesoporous carbon which had a decrease in *j* of ~14 % after 15,000 s [83]. The hollow mesoporous carbon spheres reported by Cao et al. suffer a loss of ~20.8 % in *j* after 9 h testing [84].

Fig. 6 c) shows the LSV curves after ADT of the CC-based electrocatalysts and Pt/C. Notoriously, CC_{1U} shows an improved catalytic activity after the ADT of 3000 cycles compared to its first cycle in terms of

Table 2
Surface chemical elemental composition of the electrocatalysts by XPS.

Electrocatalysts	C	O (at. %)	N
CC_0	91.43	8.16	0.41
CC_{1U}	89.65	8.54	1.81
CC_{2U}	87.69	10.56	1.75
CC_{3U}	88.46	9.93	1.61
CC_{4U}	90.44	8.06	1.50

E_{onset}, $E_{1/2}$, and j_{max} (Table 3), surpassing the rest of the CC-based electrocatalysts. Such parameters at CC_{1U} become close to those of Pt/C, which undergoes some degradation after ADT. A more detailed comparison of the performance of CC_{1U} and Pt/C at the 1st and 3000th cycles is shown in Fig. 6 d). The enhanced performance of CC_{1U} after ADT may be due to the activation of inert electrons in the sp^2 carbon nanodomains, promoted by the presence of N-species [19].

Fig. 7 a) shows the I_R collected during the ORR at 1600 rpm at the electrocatalysts. Pt/C has a characteristic behavior. Meanwhile, the N-doped CC-based electrocatalysts generate lower I_R values than Pt/C over the potential interval. The low I_R collected, particularly from CC_{1U}, suggests a small production of the $\%HO_2^-$ intermediate which is related to a reaction mechanism following a $4e^-$ transfer pathway [85].

Fig. 7 b and c) show the *n* and $\%HO_2^-$ plots before ADT of the CC-based electrocatalysts, estimated from equations (4) and (5), respectively. Fig. 7 d and e) are zooms from the highlighted yellow square from Fig. 7 b and c) respectively. CC_{1U} produces less $\%HO_2^-$ (1.01 % at 0.5 V) with a higher n (3.97) at 0.5 V vs. RHE than the other carbon electrocatalysts (Table 3). After ADT, these parameters improve at CC_{1U}, approaching those of Pt/C. Fig. 7 f) shows a comparison of the E_{onset} and $E_{1/2}$ values of the N-doped CC-based electrocatalysts before and after ADT. Although an increment in catalytic activity for the ORR after ADT is observed at some of these CC-based electrocatalysts, CC_{1U} shows the highest performance. Figure S11 shows the *n* and $\%HO_2^-$ curves of the electrocatalysts after ADT.

Considering the results in this study, the presence of N-graphitic, N-pyrrolic, and N-pyridinic species in the CC-based electrocatalysts strongly influences their catalytic activity for the ORR in two ways: 1) by promoting changes in their structural features, and 2) by increasing the presence of active sites for the adsorption of O-species which suggest a synergistic electronic effect between C and O [86]. Among them, it has been reported that N-pyridinic and N-graphitic promote the catalytic

Table 3
Electrochemical parameters of the electrocatalysts compared to Pt/C.

Electrocatalysts	E_{onset} (V vs. RHE)		$E_{1/2}$ (V vs. RHE)		j_{max} (mA cm^{-2})		HO_2^- at 0.5 V (%)		*n* at 0.5 V	
	1st	3000th	1st	3000th	1st	3000th	1st	3000th	1st	3000th
CC_0	0.81	0.78	0.50	0.52	−2.91	−2.84	7.52	4.17	3.85	3.91
CC_{1U}	0.97	0.99	0.70	0.77	−3.22	−3.65	1.01	0.96	3.97	3.98
CC_{2U}	0.91	0.91	0.65	0.66	−4.07	−3.74	1.80	1.27	3.96	3.97
CC_{3U}	0.87	0.86	0.51	0.47	−3.01	−2.69	1.70	1.50	3.95	3.96
CC_{4U}	0.92	0.94	0.63	0.65	−3.44	−3.36	1.03	1.13	3.96	3.97
Pt/C	0.99	0.97	0.85	0.83	−4.20	−3.28	0.20	0.34	3.99	3.99

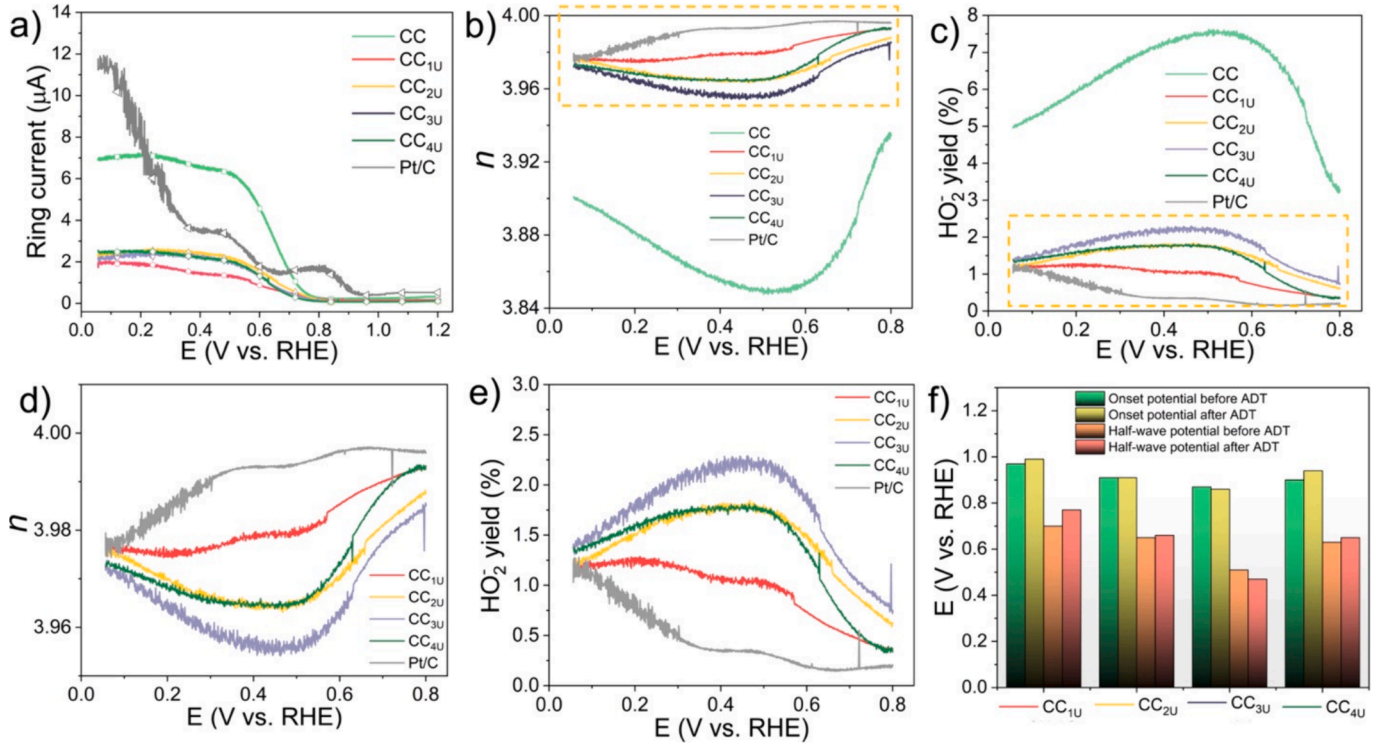

Fig. 7. a) I_R; b-c) *n* curves and overall $\%HO_2^-$ production before ADT; d) zoom of the yellow square highlighted in Figure b, e) zoom of the yellow square highlighted in Figure c, and f) comparison of E_{onset} and $E_{1/2}$ before and after ADT of the CC-based electrocatalysts, at 1600 rpm. (For interpretation of the references to colour in this figure legend, the reader is referred to the web version of this article.)

activity of carbon-based electrocatalysts for the ORR [87]. Nonetheless, these species play different roles in catalyzing the ORR. For example, N-pyridinic enhances a $2e^-$ into a $4e^-$ transfer mechanism supported by the presence of neighboring Lewis base carbon atoms [88]. Meanwhile, N-graphitic promotes the direct $4e^-$ transfer mechanism by synergistically improving an electron transfer from C to O in the presence of N atoms [89]. Therefore, the concentration of N-pyridinic or N-graphitic species strongly influences the ORR performance of carbon-based electrocatalysts.

In these studies, CC_{1U} shows macropores and mesopores, the highest SSA value, and the presence of mostly N-graphitic and N-pyrrolic species. With such features, it has the highest ORR performance. On the other hand, CC_{2U} shows a higher concentration of N-pyridinic and N-pyrrolic, CC_{3U} more N-pyridinic and CC_{4U} more N-pyridinic and N-graphitic, compared to CC_{1U}. Thus, it is hypothesized that the electron transfer from C to O atoms by N-graphitic, coupled with the N-pyrrolic enhances the ORR performance of CC_{1U} in alkaline medium [90].

Figure S12 shows the mass catalytic activity of Pt/C and the CC-based electrocatalysts a) before and b) after ADT at 1600 rpm. The slopes were obtained in the 0.95–0.75 V vs. RHE range considering the procedure reported in [91] for Pt/C and in [92] for metal-free electrocatalysts. Before ADT, Pt/C show a Tafel slope of 62 mV dec^{-1}, an expected value at low overpotentials [93]. Overall, the CC-based electrocatalysts show a lower mass catalytic activity than Pt/C. Before ADT, CC_{1U} outperforms the rest of the CC-based electrocatalysts. Nevertheless, their relatively low Tafel slopes demonstrate the fast kinetics of the ORR at their surface. After ADT, the mass performance of the CC-based electrocatalysts remains stable with variations of ~3 mV dec^{-1}, compared to Pt/C (6 mV dec^{-1} drop). The decrease of I_M values at low overpotential after ADT demonstrates a Temkin mechanism which involves a higher adsorption of O-species [94] making consistent the mass catalytic activity, I_R, *n,* and $\%HO_2^-$ results.

4. Conclusions

In this work, a systematic study of the effects promoted by modifying the concentration of urea in CC derived ORR electrocatalysts was studied for the first time. It was shown that by increasing the urea concentration, the pore size decreases, while the $d_{(0\,0\,2)}$ interplanar distance and the *j* increases due to the electrochemical double layer of CC_0. With CC:urea 1:1 and 1:2 ratios, the formation of active C-N bonds was promoted, while an increase in urea concentration inhibits the formation of species which promotes the ORR. The CC_{1U} electrocatalysts showed the highest catalytic activity among the CC-based electrocatalysts, with values before ADT of $E_{onset} = 0.97$ V vs. RHE, $E_{1/2} = 0.7$ V vs. RHE, and $j_{max} = -3.22$ mA cm^{-2}. CC_{1U} also had the lowest $\%HO_2^-$ (1.01) and highest *n* (3.97) both at 0.5 V vs. RHE. After ADT, CC_{1U} showed high electrochemical stability, with improved parameters of the ORR, a behavior ascribed to the activation of inert π electrons in sp^2 nanodomains promoted by the doping with N-species. Furthermore, CC_{1U} has the higher SSA compared to CC_0, CC_{2U}, CC_{3U}, and CC_{4U}. To conclude, we think this work shows that it is possible to design active electrocatalysts for energy conversion reactions, with controlled doping levels, by using readily available reagents, simple and less polluting methodologies, and above all thinking that, sometimes, less is more.

CRediT authorship contribution statement

J.C. Martínez-Loyola: Writing – review & editing, Writing – original draft, Validation, Methodology, Investigation, Data curation, Conceptualization. **M.A. Carrasco-Cordero:** Methodology, Investigation. **I.L. Alonso-Lemus:** Writing – review & editing, Supervision. **F.J. Rodríguez-Varela:** Writing – review & editing, Supervision. **P. Bartolo-Pérez:** Writing – review & editing, Resources. **B. Escobar-Morales:** Writing – review & editing, Resources. **Y.I. Vega-Cantú:** Writing – review & editing, Supervision, Project administration. **F.J. Rodríguez-Macías:** Writing – review & editing, Supervision.

Declaration of competing interest

The authors declare that they have no known competing financial interests or personal relationships that could have appeared to influence the work reported in this paper.

Data availability

Data will be made available on request.

Acknowledgements

JCML acknowledges his Ph.D. scholarship awarded by Mexico's National Council for Humanities, Science and Technology (CONAHCyT). FJRM acknowledges funding by CONAHCYT through the "Fondo Sectorial de Investigación para la Educación" (Grant A1-S-43933).

Appendix A. Supplementary material

Supplementary data to this article can be found online at https://doi.org/10.1016/j.elecom.2024.107792.

References

[1] O.O. Fashedemi, A. Bello, T. Adebusuyi, S. Bindir, Recent trends in Carbon support for improved performance of Alkaline Fuel cells, Curr. Opin. Electrochem. (2022) 101132, https://doi.org/10.1016/j.coelec.2022.101132.
[2] M.M. Hossen, M.S. Hasan, M.R.I. Sardar, J. bin Haider, Mottakin, K. Tammeveski, P. Atanassov, State-of-the-art and developmental trends in platinum group metal-free cathode catalyst for anion exchange membrane fuel cell (AEMFC), Appl. Catal. B Environ. 325 (2023) 121733. doi: 10.1016/j.apcatb.2022.121733.
[3] V. Das, S. Padmanaban, K. Venkitusamy, R. Selvamuthukumaran, F. Blaabjerg, P. Siano, Recent advances and challenges of fuel cell based power system architectures and control – A review, Renew. Sustain. Energy Rev. 73 (2017) 10–18, https://doi.org/10.1016/j.rser.2017.01.148.
[4] H. Cruz-Martínez, H. Rojas-Chávez, P.T. Matadamas-Ortiz, J.C. Ortiz-Herrera, E. López-Chávez, O. Solorza-Feria, D.I. Medina, Current progress of Pt-based ORR electrocatalysts for PEMFCs: An integrated view combining theory and experiment, Mater. Today Phys. 19 (2021) 100406, https://doi.org/10.1016/j.mtphys.2021.100406.
[5] O.Z. Sharaf, M.F. Orhan, An overview of fuel cell technology: Fundamentals and applications, Renew. Sustain. Energy Rev. 32 (2014) 810–853, https://doi.org/10.1016/j.rser.2014.01.012.
[6] T. Jacob, The mechanism of forming H_2O from H_2 and O_2 over a Pt catalyst via direct oxygen reduction, Fuel Cells 6 (2006) 159–181, https://doi.org/10.1002/fuce.200500201.
[7] H. Cruz-Martínez, M.M. Tellez-Cruz, O.X. Guerrero-Gutiérrez, C.A. Ramírez-Herrera, M.G. Salinas-Juárez, A. Velázquez-Osorio, O. Solorza-Feria, Mexican contributions for the improvement of electrocatalytic properties for the oxygen reduction reaction in PEM fuel cells, Int. J. Hydrogen Energy. 44 (2019) 12477–12491, https://doi.org/10.1016/j.ijhydene.2018.05.168.
[8] J. Quílez-Bermejo, E. Morallón, D. Cazorla-Amorós, Metal-free heteroatom-doped carbon-based catalysts for ORR: A critical assessment about the role of heteroatoms, Carbon N. Y. 165 (2020) 434–454, https://doi.org/10.1016/j.carbon.2020.04.068.
[9] A. Dessalle, J. Quílez-Bermejo, V. Fierro, F. Xu, A. Celzard, Recent progress in the development of efficient biomass-based ORR electrocatalysts, Carbon N. Y. 203 (2023) 237–260, https://doi.org/10.1016/j.carbon.2022.11.073.
[10] T. Zhang, H. Wang, J. Zhang, J. Ma, Z. Wang, J. Liu, X. Gong, Carbon charge population and oxygen molecular transport regulated by program-doping for highly efficient 4e-ORR, Chem. Eng. J. 444 (2022) 136560, https://doi.org/10.1016/j.cej.2022.136560.
[11] Z. Chen, W. Wei, L. Song, B.-J. Ni, Hybrid water electrolysis: A new sustainable avenue for energy-saving hydrogen production, Sustain. Horizons. 1 (2022) 100002, https://doi.org/10.1016/j.horiz.2021.100002.
[12] M. Borghei, N. Laocharoen, E. Kibena-Põldsepp, L.-S. Johansson, J. Campbell, E. Kauppinen, K. Tammeveski, O.J. Rojas, Porous N, P-doped carbon from coconut shells with high electrocatalytic activity for oxygen reduction: Alternative to Pt-C for alkaline fuel cells, Appl. Catal. B Environ. 204 (2017) 394–402, https://doi.org/10.1016/j.apcatb.2016.11.029.
[13] X.-L. Zhou, H. Zhang, L.-M. Shao, F. Lü, P.-J. He, Preparation and application of hierarchical porous carbon materials from waste and biomass: A review, Waste Biomass Valoriz. 12 (2021) 1699–1724, https://doi.org/10.1007/s12649-020-01109-y.

[14] R. Zhao, Y. Chen, S. Huang, Doping engineering on carbons as electrocatalysts for oxygen reduction reaction, Fundam. Res. 1 (2021) 807–823, https://doi.org/10.1016/j.fmre.2021.06.021.

[15] H. Yuan, H. Chen, D. Li, L. Deng, J. Chen, Y. Fan, M. He, F. Sun, Catalytic synthesis and simultaneous co-doping of hierarchically porous carbon with in-situ coated graphene from biomass tar as efficient catalyst for ORR, Electrochem. Commun. 100 (2019) 52–59, https://doi.org/10.1016/j.elecom.2019.01.021.

[16] Y. Zhao, X. Liu, Y. Liu, Y. Chen, S. Gao, Favorable pore size distribution of biomass-derived N, S dual-doped carbon materials for advanced oxygen reduction reaction, Int. J. Hydrogen Energy. 47 (2022) 12964–12974, https://doi.org/10.1016/j.ijhydene.2022.02.064.

[17] H. Xu, J. Yang, R. Ge, J. Zhang, Y. Li, M. Zhu, L. Dai, S. Li, W. Li, Carbon-based bifunctional electrocatalysts for oxygen reduction and oxygen evolution reactions: Optimization strategies and mechanistic analysis, J. Energy Chem. 71 (2022) 234–265, https://doi.org/10.1016/j.jechem.2022.03.022.

[18] L. Yang, J. Shui, L. Du, Y. Shao, J. Liu, L. Dai, Z. Hu, Carbon-based metal-free ORR electrocatalysts for fuel cells: Past, present, and future, Adv. Mater. 31 (2019) 1804799, https://doi.org/10.1002/adma.201804799.

[19] F. An, X. Bao, X. Deng, Z. Ma, X. Wang, Carbon-based metal-free oxygen reduction reaction electrocatalysts: Past, present and future, New Carbon Mater. 37 (2022) 338–354, https://doi.org/10.1016/S1872-5805(22)60590-0.

[20] D. Li, Y. Qu, S. Li, M. Wei, Y. Liu, A novel honeycomb Fe-N-C composition derived from wheat flour as an efficiency catalyst for the oxygen reduction reaction, J. Solid State Electrochem. 24 (2020) 1105–1112, https://doi.org/10.1007/s10008-020-04578-2.

[21] M. Dhelipan, A. Arunchander, A.K. Sahu, D. Kalpana, Activated carbon from orange peels as supercapacitor electrode and catalyst support for oxygen reduction reaction in proton exchange membrane fuel cell, J. Saudi Chem. Soc. 21 (2017) 487–494, https://doi.org/10.1016/j.jscs.2016.12.003.

[22] Y. Sun, R. Zhong, H. Zhang, T. Huang, J. Yu, H. Fang, D. Liang, Z. Guo, Soybean milk derived carbon intercalated with reduced graphene oxide as high efficient electrocatalysts for oxygen reduction reaction, Int. J. Hydrogen Energy. 44 (2019) 21790–21802, https://doi.org/10.1016/j.ijhydene.2019.06.174.

[23] D. Kong, L. Liu, W. Yuan, A. Xie, Y. Shen, Facile synthesis and excellent catalytic performance of nitrogen-doped porous carbons derived from banana peel towards oxygen reduction reaction, Mater. Res. Bull. 103 (2018) 63–69, https://doi.org/10.1016/j.materresbull.2018.03.019.

[24] I.L. Alonso-Lemus, B. Escobar-Morales, D. Lardizabal-Gutierrez, L. de la Torre-Saenz, P. Quintana-Owen, F.J. Rodriguez-Varela, Short communication: Onion skin waste-derived biocarbon as alternative non-noble metal electrocatalyst towards ORR in alkaline media, Int. J. Hydrogen Energy. 44 (2019) 12409–12414, https://doi.org/10.1016/j.ijhydene.2018.10.050.

[25] J. Shi, N. Lin, H. Lin, J. Yang, W. Zhang, A N-doped rice husk-based porous carbon as an electrocatalyst for the oxygen reduction reaction, New Carbon Mater. 35 (2020) 401–409, https://doi.org/10.1016/S1872-5805(20)60497-8.

[26] M.O. Torres-Fuentez, Y.M. Maldonado, I.L. Alonso-Lemus, F.J. Rodríguez-Varela, Biomass-Derived Electroactive Carbons with Application in Green Electrochemical Technologies, in: Noble Met. Electrocatal. Fundam. Recent Adv. Electrocatal. Energy Appl. Vol. 1, American Chemical Society, 2022: pp. 129-164 SE–6. doi:doi: 10.1021/bk-2022-1431.ch006.

[27] P. Manasa, S. Sambasivam, F. Ran, Recent progress on biomass waste derived activated carbon electrode materials for supercapacitors applications—A review, J. Energy Storage 54 (2022) 105290, https://doi.org/10.1016/j.est.2022.105290.

[28] S.K. Tiwari, M. Bystrzejewski, A. De Adhikari, A. Huczko, N. Wang, Methods for the conversion of biomass waste into value-added carbon nanomaterials: Recent progress and applications, Prog. Energy Combust. Sci. 92 (2022) 101023, https://doi.org/10.1016/j.pecs.2022.101023.

[29] Foreign Agricultural Service, U.S. Departament of Agriculture, Corn world production, https://ipad.fas.usda.gov/cropexplorer/cropview/commodityView.aspx?cropid=0440000, (accessed July 18, 2024).

[30] Statista, Global corn production in 2023/2024, by country, https://www.statista.com/statistics/254292/global-corn-production-by-country/, (accessed July 18, 2024).

[31] Secretaría de Agrigultura y Desarrollo Rural, Maíz cultivo de México, (2023). https://www.gob.mx/agricultura/articulos/maiz-cultivo-de-mexico (accessed July 18, 2024).

[32] Servicio de Información Agroalimentaria y Pesquera (SIAP) , "Panorama Agroalimentario 2023". Publication by the Agri-Food and Fisheries Information Service (SIAP) of the Secretariat for Agriculture and Rural Development (*Secretaría de Agricultura y Desarrollo Rural*) of the Mexican Government. Available online at https://www.gob.mx/siap/acciones-y-programas/panorama-agroalimentario-258035 (accessed July 18, 2024).

[33] S.O. Serna-Saldivar, E. Perez Carrillo, Chapter 16 - Food Uses of Whole Corn and Dry-Milled Fractions, in: S.O. Serna-Saldivar (Ed.), Corn (Third Ed., Third Edit, AACC International Press, Oxford, 2019: pp. 435–467. doi: 10.1016/B978-0-12-811971-6.00016-4.

[34] G.E. Varvel, W.W. Wilhelm, Cob biomass production in the Western Corn Belt, BioEnergy Res. 1 (2008) 223–228, https://doi.org/10.1007/s12155-008-9026-6.

[35] D. Pennington, Chapter 7 - Bioenergy crops, in: A. Dahiya (Ed.), Bioenergy (Second Ed., Second Edi, Academic Press, 2020: pp. 133–155. doi: 10.1016/B978-0-12-815497-7.00007-5.

[36] S.K. Das, A. Kesh, S. Akula, A.K. Sahu, N-, F-, and Fe-Doped Mesoporous Carbon Derived from Corncob Waste and Creating Oxygen Reduction Reaction Active Centers with a Maximum Charge Density of ≥0.25 for a Polymer Electrolyte Fuel Cell Catalyst, Energy & Fuels. 36 (2022) 2108–2122. doi:10.1021/acs.energyfuels.1c03174.

[37] W. Yan, Y. Wu, Y. Chen, Q. Liu, K. Wang, N. Cao, F. Dai, X. Li, J. Jiang, Facile preparation of N-doped corncob-derived carbon nanofiber efficiently encapsulating Fe2O3 nanocrystals towards high ORR electrocatalytic activity, J. Energy Chem. 44 (2020) 121–130, https://doi.org/10.1016/j.jechem.2019.09.002.

[38] Y. Wu, Q. Hou, F. Qiu, M. Qi, C. Sun, Y. Chen, $Co_2O_3/Co_2N_{0.67}$ nanoparticles encased in honeycomb-like N{,} P{,} O-codoped carbon framework derived from corncob as efficient ORR electrocatalysts, RSC Adv. 12 (2022) 207–215, https://doi.org/10.1039/D1RA07017G.

[39] S. Zheng, R. Chen, J. Yang, J. Guo, W. An, J. Tang, Biomass-derived nitrogen-doped carbons activated by zinc halides for electrocatalytic oxygen reduction reaction, Int. J. Hydrogen Energy 58 (2024) 333–340, https://doi.org/10.1016/j.ijhydene.2024.01.217.

[40] C. Ling, W.-Y. Xie, S.-F. He, G.-C. Liang, X.-Y. Xiao, C.-L. Yang, H.-Y. Liu, Si-doped biomass carbon supported Fe-N-C catalyst derived from pyrolysis of iron porphyrin for oxygen reduction reaction, J. Alloys Compd. 987 (2024) 174172, https://doi.org/10.1016/j.jallcom.2024.174172.

[41] S. Zhao, C. Wang, L. Cai, Y. Chen, W. Sun, Z. Zhu, A gasification strategy to anchor Fe, Ni dual-sites on biomass-derived N, P co-doped porous carbon as an efficient bifunctional catalyst for Zn-air batteries, Sustain. Mater. Technol. 40 (2024) e00875, https://doi.org/10.1016/j.susmat.2024.e00875.

[42] W. Yan, Y. Zhao, L. Zhang, R. Wang, S. Cui, Biomass-derived Co, N and P co-doped 3D porous carbon as an effective electrocatalyst for oxygen reduction reaction, Mater. Lett. 357 (2024) 135812, https://doi.org/10.1016/j.matlet.2023.135812.

[43] M.N. Efimov, D.G. Muratov, A.L. Klyuev, N.A. Zhilyaeva, A.A. Vasilev, S.Z. Ozkan, G.P. Karpacheva, Ultrasonic treatment duration: A nuanced parameter in synthesis affecting structural properties and ORR performance of KOH-activated carbon, Diam. Relat. Mater. 142 (2024) 110804, https://doi.org/10.1016/j.diamond.2024.110804.

[44] X. Zhao, X. Maimaitiyiming, M. Tursun, H. Lin, Preparation of Fe single-atom carbon materials for DMFC and ZAB cathodic ORR catalysts based on the natural corn stalk binder/corn stalk biomass composite, Fuel 364 (2024) 131089, https://doi.org/10.1016/j.fuel.2024.131089.

[45] Z. Yang, B. Ma, Y. Zhou, Atomically dispersed iron catalyst supported on nitrogen doped biomass aerogels for high-performance rechargeable zinc-air batteries, Fuel 371 (2024) 132119, https://doi.org/10.1016/j.fuel.2024.132119.

[46] H.-W. Liang, X. Zhuang, S. Brüller, X. Feng, K. Müllen, Hierarchically porous carbons with optimized nitrogen doping as highly active electrocatalysts for oxygen reduction, Nat. Commun. 5 (2014) 4973, https://doi.org/10.1038/ncomms5973.

[47] N. Sumangala Devi, M. Hariram, S. Vivekanandhan, Modification techniques to improve the capacitive performance of biocarbon materials, J Energy Storage 33 (2021) 101870, https://doi.org/10.1016/j.est.2020.101870.

[48] L. Bouleau, S. Pérez-Rodríguez, J. Quílez-Bermejo, M.T. Izquierdo, F. Xu, V. Fierro, A. Celzard, Best practices for ORR performance evaluation of metal-free porous carbon electrocatalysts, Carbon N. Y. 189 (2022) 349–361, https://doi.org/10.1016/j.carbon.2021.12.078.

[49] S.M. Alia, C. Ngo, S. Shulda, M.-A. Ha, A.A. Dameron, J.N. Weker, K.C. Neyerlin, S. S. Kocha, S. Pylypenko, B.S. Pivovar, Exceptional oxygen reduction reaction activity and durability of platinum-nickel nanowires through synthesis and post-treatment optimization, ACS Omega 2 (2017) 1408–1418, https://doi.org/10.1021/acsomega.7b00054.

[50] G.A. Ferrero, A.B. Fuertes, M. Sevilla, M.-M. Titirici, Efficient metal-free N-doped mesoporous carbon catalysts for ORR by a template-free approach, Carbon N. Y. 106 (2016) 179–187, https://doi.org/10.1016/j.carbon.2016.04.080.

[51] J.P. Paraknowitsch, A. Thomas, Doping carbons beyond nitrogen: an overview of advanced heteroatom doped carbons with boron{,} sulphur and phosphorus for energy applications, Energy Environ. Sci. 6 (2013) 2839–2855, https://doi.org/10.1039/C3EE41444B.

[52] R. Dong, F. Wu, Y. Bai, Q. Li, X. Yu, Y. Li, Q. Ni, C. Wu, Tailoring defects in hard carbon anode towards enhanced Na storage performance, Energy Mater. Adv. 2022 (2022) 9896218, https://doi.org/10.34133/2022/9896218.

[53] T. Qiu, J.-G. Yang, X.-J. Bai, Y.-L. Wang, The preparation of synthetic graphite materials with hierarchical pores from lignite by one-step impregnation and their characterization as dye absorbents, RSC Adv. 9 (2019) 12737–12746, https://doi.org/10.1039/C9RA00343F.

[54] S. Ali, M. Rizwan, M.B. Shakoor, A. Jilani, R. Anjum, High sorption efficiency for As(III) and As(V) from aqueous solutions using novel almond shell biochar, Chemosphere 243 (2020) 125330, https://doi.org/10.1016/j.chemosphere.2019.125330.

[55] T. Liu, Y. Guo, N. Peng, Q. Lang, Y. Xia, C. Gai, Z. Liu, Nitrogen transformation among char, tar and gas during pyrolysis of sewage sludge and corresponding hydrochar, J. Anal. Appl. Pyrolysis 126 (2017) 298–306, https://doi.org/10.1016/j.jaap.2017.05.017.

[56] Z. Zhang, L. Li, Y. Qing, X. Lu, Y. Wu, N. Yan, W. Yang, Hierarchically interconnected N-doped carbon aerogels derived from cellulose nanofibrils as high performance and stable electrodes for supercapacitors, J. Phys. Chem. C 122 (2018) 23852–23860, https://doi.org/10.1021/acs.jpcc.8b06550.

[57] J. Lang, L. Matějová, A.K. Cuentas-Gallegos, D.R. Lobato-Peralta, K. Ainassaari, M. M. Gómez, J.L. Solís, D. Mondal, R.L. Keiski, G.J.F. Cruz, Evaluation and selection of biochars and hydrochars derived from agricultural wastes for the use as adsorbent and energy storage materials, J. Environ. Chem. Eng. 9 (2021) 105979, https://doi.org/10.1016/j.jece.2021.105979.

[58] S. Wang, L. Dong, Z. Li, N. Lin, H. Xu, S. Gao, Sustainable supercapacitors of nitrogen-doping porous carbon based on cellulose nanocrystals and urea, Int. J. Biol. Macromol. 164 (2020) 4095–4103, https://doi.org/10.1016/j.ijbiomac.2020.09.011.

[59] C. Wang, Y. Li, X. He, Y. Ding, Q. Peng, W. Zhao, E. Shi, S. Wu, A. Cao, Cotton-derived bulk and fiber aerogels grafted with nitrogen-doped graphene, Nanoscale 7 (2015) 7550–7558, https://doi.org/10.1039/c5nr00996k.
[60] L. Bokobza, J.-L. Bruneel, M. Couzi, Raman Spectra of Carbon-Based Materials (from Graphite to Carbon Black) and of Some Silicone Composites, C. 1 (2015) 77–94. doi:10.3390/c1010077.
[61] D. Kumbhar, A. Palliyarayil, D. Reghu, D. Shrungar, S. Umapathy, S. Sil, Rapid discrimination of porous bio-carbon derived from nitrogen rich biomass using Raman spectroscopy and artificial intelligence methods, Carbon N. Y. 178 (2021) 792–802, https://doi.org/10.1016/j.carbon.2021.03.064.
[62] M. Pawlyta, J.-N. Rouzaud, S. Duber, Raman microspectroscopy characterization of carbon blacks: Spectral analysis and structural information, Carbon N. Y. 84 (2015) 479–490, https://doi.org/10.1016/j.carbon.2014.12.030.
[63] A. Jorio, M.A. Pimenta, A.G.S. Filho, R. Saito, G. Dresselhaus, M.S. Dresselhaus, Characterizing carbon nanotube samples with resonance Raman scattering, New J. Phys. 5 (2003) 139, https://doi.org/10.1088/1367-2630/5/1/139.
[64] Q. Du, Y. Zhao, Y. Chen, J. Liu, H. Li, G. Bai, K. Zhuo, J. Wang, Nitrogen-doped porous carbon nanosheets as both anode and cathode for advanced potassium-ion hybrid capacitors, Green Energy Environ. 8 (2023) 579–588, https://doi.org/10.1016/j.gee.2022.02.013.
[65] C. Chang, M. Li, H. Wang, S. Wang, X. Liu, H. Liu, L. Li, A novel fabrication strategy for doped hierarchical porous biomass-derived carbon with high microporosity for ultrahigh-capacitance supercapacitors, J. Mater. Chem. A 7 (2019) 19939–19949, https://doi.org/10.1039/C9TA06210F.
[66] Y.-L. Zhang, S.-Y. Li, Z.-S. Tang, Z. Song, J. Sun, Xanthoceras sorbifolia seed coats derived porous carbon with unique architecture for high rate performance supercapacitors, Diam. Relat. Mater. 91 (2019) 119–126, https://doi.org/10.1016/j.diamond.2018.11.013.
[67] Z. Ling, Z. Wang, M. Zhang, C. Yu, G. Wang, Y. Dong, S. Liu, Y. Wang, J. Qiu, Sustainable synthesis and assembly of biomass-derived B/N Co-doped carbon nanosheets with ultrahigh aspect ratio for high-performance supercapacitors, Adv. Funct. Mater. 26 (2016) 111–119, https://doi.org/10.1002/adfm.201504004.
[68] M. Chen, J. Chen, C. Jia, J. Luo, Z. Yang, J. Chung-Yen Jung, J. Zhang, S. Chen, S. Zhang, Metal-free carbon semi-tubes for oxygen reduction electrocatalysis, Cell Reports Phys. Sci. 4 (2023) 101204, https://doi.org/10.1016/j.xcrp.2022.101204.
[69] N.S. Pinky, M. Bin Mobarak, S. Mustafi, M. Zesanur Rahman, A. Nahar, T. Saha, N. Mohammed Bahadur, Facile preparation of micro-porous biochar from Bangladeshi sprouted agricultural waste (corncob) via in-house built heating chamber for cationic dye removal, Arab. J. Chem. 16 (2023) 105080, https://doi.org/10.1016/j.arabjc.2023.105080.
[70] Z. Jian, C. Bommier, L. Luo, Z. Li, W. Wang, C. Wang, P.A. Greaney, X. Ji, Insights on the mechanism of Na-ion storage in soft carbon anode, Chem. Mater. 29 (2017) 2314–2320, https://doi.org/10.1021/acs.chemmater.6b05474.
[71] C. del M. Saavedra Rios, L. Simonin, A. de Geyer, C. Matei Ghimbeu, C. Dupont, Unraveling the Properties of Biomass-Derived Hard Carbons upon Thermal Treatment for a Practical Application in Na-Ion Batteries, Energies. 13 (2020). doi: 10.3390/en13143513.
[72] S. He, M. Li, X. Lin, T. Li, F. Tan, S. Hao, Z. Yang, L. Cui, C. Sun, Y. Xu, Y. Ke, D. Zhu, D. Chen, Superior electrocatalytic ORR performance of Melaleuca Leucadendron L barks derived hierarchical porous carbon with abundant atom-scale vacancies and multiheteroatoms, Ceram. Int. 48 (2022) 11111–11123, https://doi.org/10.1016/j.ceramint.2021.12.331.
[73] X. Chen, W. Zhang, Y. Qu, X. Chen, Y. Liu, C. Lu, Solvent-free synthesis of honeycomb-like N-doped porous carbon derived from biomass pine sawdust as an efficient metal-free electrocatalyst for oxygen reduction reaction, J. Electroanal. Chem. (2022) 116909, https://doi.org/10.1016/j.jelechem.2022.116909.
[74] L. Yang, H. Ding, G. Xu, L. Zhang, B. Wei, Efficient ORR activity of N-doped porous carbon encapsulated cobalt electrocatalyst derived from a novel bimetal-organic framework, Mater. Res. Bull. 138 (2021) 111237, https://doi.org/10.1016/j.materresbull.2021.111237.
[75] T. Li, D. Chen, L. Gu, S. Chen, C. Li, J. Liao, Y. Zhou, Y. Xu, C. Sun, Z. Yang, H. Yang, Single-source precursor synthesis of nitrogen-doped porous carbon for high-performance electrocatalytic ORR application, Ceram. Int. 45 (2019) 8354–8361, https://doi.org/10.1016/j.ceramint.2019.01.143.
[76] C.L. Chiang, J.M. Yang, 11 - Flame retardance and thermal stability of polymer/graphene nanosheet oxide composites, in: D.-Y. Wang (Ed.), Nov. Fire Retard. Polym. Compos. Mater., Woodhead Publishing, 2017: pp. 295–312. doi: 10.1016/B978-0-08-100136-3.00011-X.
[77] L. Liu, G. Zeng, J. Chen, L. Bi, L. Dai, Z. Wen, N-doped porous carbon nanosheets as pH-universal ORR electrocatalyst in various fuel cell devices, Nano Energy 49 (2018) 393–402, https://doi.org/10.1016/j.nanoen.2018.04.061.
[78] Y. Fang, Q. Zhang, D. Zhang, L. Cui, The synthesis of porous carbons from a lignin-rich residue for high-performance supercapacitors, New Carbon Mater. 37 (2022) 743–751, https://doi.org/10.1016/S1872-5805(21)60058-6.
[79] Z.-A. Qiao, B. Guo, A.J. Binder, J. Chen, G.M. Veith, S. Dai, Controlled synthesis of mesoporous carbon nanostructures via a "Silica-Assisted" strategy, Nano Lett. 13 (2013) 207–212, https://doi.org/10.1021/nl303889h.
[80] P. Wei, X. Li, Z. He, X. Sun, Q. Liang, Z. Wang, C. Fang, Q. Li, H. Yang, J. Han, Y. Huang, Porous N, B co-doped carbon nanotubes as efficient metal-free electrocatalysts for ORR and Zn-air batteries, Chem. Eng. J. 422 (2021) 130134, https://doi.org/10.1016/j.cej.2021.130134.
[81] L. Sun, Y. Gong, D. Li, C. Pan, Biomass-derived porous carbon materials: synthesis, designing, and applications for supercapacitors, Green Chem. 24 (2022) 3864–3894, https://doi.org/10.1039/d2gc00099g.
[82] Y. Xi, Z. Xiao, H. Lv, H. Sun, X. Wang, Z. Zhao, S. Zhai, Q. An, Template-assisted synthesis of porous carbon derived from biomass for enhanced supercapacitor performance, Diam. Relat. Mater. 128 (2022) 109219, https://doi.org/10.1016/j.diamond.2022.109219.
[83] S. Cao, W. Shang, G.-L. Li, Z.-F. Lu, X. Wang, Y. Yan, C. Hao, S. Wang, G. Sun, Defect-rich and metal-free N, S co-doped 3D interconnected mesoporous carbon material as an advanced electrocatalyst towards oxygen reduction reaction, Carbon N. Y. 184 (2021) 127–135, https://doi.org/10.1016/j.carbon.2021.08.003.
[84] W. Xiong, H. Li, R. Cao, Nitrogen and sulfur dual-doped hollow mesoporous carbon spheres as efficient metal-free catalyst for oxygen reduction reaction, Inorg. Chem. Commun. 114 (2020) 107848, https://doi.org/10.1016/j.inoche.2020.107848.
[85] G. Zhong, Z. Meng, M. Xu, H. Xie, S. Xu, X. Fu, W. Liao, S. Zheng, Y. Xu, Self-nitrogen-doped porous carbon prepared via pyrolysis of grass-blade without additive for oxygen reduction reaction, Diam. Relat. Mater. 121 (2022) 108742, https://doi.org/10.1016/j.diamond.2021.108742.
[86] J. Sun, S.E. Lowe, L. Zhang, Y. Wang, K. Pang, Y. Wang, Y. Zhong, P. Liu, K. Zhao, Z. Tang, H. Zhao, Ultrathin nitrogen-doped holey carbon@graphene bifunctional electrocatalyst for oxygen reduction and evolution reactions in alkaline and acidic media, Angew. Chem. Int. Ed. 57 (2018) 16511–16515, https://doi.org/10.1002/anie.201811573.
[87] D. Guo, R. Shibuya, C. Akiba, S. Saji, T. Kondo, J. Nakamura, Active sites of nitrogen-doped carbon materials for oxygen reduction reaction clarified using model catalysts, Science (80-) 351 (2016) 361–365, https://doi.org/10.1126/science.aad0832.
[88] M. Skorupska, A. Ilnicka, J.P. Lukaszewicz, The effect of nitrogen species on the catalytic properties of N-doped graphene, Sci. Rep. 11 (2021) 23970, https://doi.org/10.1038/s41598-021-03403-8.
[89] H. Han, Y. Noh, Y. Kim, W.S. Jung, S. Park, W.B. Kim, An N-doped porous carbon network with a multidirectional structure as a highly efficient metal-free catalyst for the oxygen reduction reaction, Nanoscale 11 (2019) 2423–2433, https://doi.org/10.1039/C8NR10242B.
[90] J. Zheng, C. Guo, C. Chen, M. Fan, J. Gong, Y. Zhang, T. Zhao, Y. Sun, X. Xu, M. Li, R. Wang, Z. Luo, C. Chen, High content of pyridinic- and pyrrolic-nitrogen-modified carbon nanotubes derived from blood biomass for the electrocatalysis of oxygen reduction reaction in alkaline medium, Electrochim. Acta 168 (2015) 386–393, https://doi.org/10.1016/j.electacta.2015.03.173.
[91] A. Hernández-Ramírez, M.E. Sánchez-Castro, I. Alonso-Lemus, K.K. Aruna, P. Karthikeyan, R. Manoharan, F.J. Rodríguez-Varela, Evaluation of the nickel titanate-modified Pt nanostructured catalyst for the ORR in Alkaline media, J. Electrochem. Soc. 163 (2015) F16, https://doi.org/10.1149/2.0161602jes.
[92] F. Jaouen, J. Herranz, M. Lefèvre, J.-P. Dodelet, U.I. Kramm, I. Herrmann, P. Bogdanoff, J. Maruyama, T. Nagaoka, A. Garsuch, J.R. Dahn, T. Olson, S. Pylypenko, P. Atanassov, E.A. Ustinov, Cross-laboratory experimental study of non-noble-metal electrocatalysts for the oxygen reduction reaction, ACS Appl. Mater. Interfaces 1 (2009) 1623–1639, https://doi.org/10.1021/am900219g.
[93] A. Holewinski, S. Linic, Elementary mechanisms in electrocatalysis: Revisiting the ORR Tafel slope, J. Electrochem. Soc. 159 (2012) H864, https://doi.org/10.1149/2.022211jes.
[94] E.J. Coleman, M.H. Chowdhury, A.C. Co, Insights into the oxygen reduction reaction activity of Pt/C and PtCu/C catalysts, ACS Catal. 5 (2015) 1245–1253, https://doi.org/10.1021/cs501762g.